Accepted: 21 August 2021

DOI: 10.1002/lsm.23473

PRECLINICAL REPORT

Toward optoacoustic sciatic nerve detection using an all-fiber interferometric-based sensor for endoscopic smart laser surgery

Hervé Nguendon Kenhagho[1] | **Ferda Canbaz**[1] | **Alois Hopf**[2] | **Raphael Guzman**[2,3] | **Philippe Cattin**[4] | **Azhar Zam**[1]

[1]Biomedical Laser and Optics Group (BLOG), Department of Biomedical Engineering, University of Basel, Allschwil, Switzerland

[2]Brain Ischemia and Regeneration, Department of Biomedicine, University Hospital of Basel, University of Basel, Basel, Switzerland

[3]Neurosurgery Group, Department of Biomedical Engineering, University of Basel, Allschwil, Switzerland

[4]Department of Biomedical Engineering, Center for Medical Image Analysis and Navigation, University of Basel, Allschwil, Switzerland

Correspondence

Hervé Nguendon Kenhagho and Azhar Zam, Biomedical Laser and Optics Group (BLOG), Department of Biomedical Engineering, University of Basel, Gewerbestr. 14, Allschwil 4123, Switzerland.
Email: herve.nguendon@unibas.ch and azhar.zam@unibas.ch

Funding information

The Werner Siemens Foundation

Abstract

Objectives: Laser surgery requires efficient tissue classification to reduce the probability of undesirable or unwanted tissue damage. This study aimed to investigate acoustic shock waves (ASWs) as a means of classifying sciatic nerve tissue.

Materials and Methods: In this study, we classified sciatic nerve tissue against other tissue types—hard bone, soft bone, fat, muscle, and skin extracted from two proximal and distal fresh porcine femurs—using the ASWs generated by a laser during ablation. A nanosecond frequency-doubled Nd:YAG laser at 532 nm was used to create 10 craters on each tissue type's surface. We used a fiber-coupled Fabry–Pérot sensor to measure the ASWs. The spectrum's amplitude from each ASW frequency band measured was used as input for principal component analysis (PCA). PCA was combined with an artificial neural network to classify the tissue types. A confusion matrix and receiver operating characteristic (ROC) analysis was used to calculate the accuracy of the testing-data-based scores from the sciatic nerve and the area under the ROC curve (AUC) with a 95% confidence-level interval.

Results: Based on the confusion matrix and ROC analysis of the model's tissue classification results (leave-one-out cross-validation), nerve tissue could be classified with an average accuracy rate and AUC result of $95.78 \pm 1.3\%$ and $99.58 \pm 0.6\%$, respectively.

Conclusion: This study demonstrates the potential of using ASWs for remote classification of nerve and other tissue types. The technique can serve as the basis of a feedback control system to detect and preserve sciatic nerves in endoscopic laser surgery.

KEYWORDS

acoustic shock signal, artificial network machine, laser ablation, principal component analysis, sciatic nerve tissue, tissue classification

INTRODUCTION

Laser surgery offers numerous advantages to both patients and surgeons, such as ablating organic tissues with high precision and achieving a functional cutting geometry with minimal trauma. Additionally, contact-free ablation of the laser allows an advanced level of sterility compared to the use of mechanical tools in surgery.[1,2] Combining laser osteotomy with endoscopy (minimally invasive surgery) will additionally push the restrictions of possible applications for the benefits of the patient—in the field of maxillo-facial-, neuro-, and orthopedic surgery.[3] However, these advantages are somewhat diminished by a lack of information on ablated tissue type and

depth. During laser ablation, it is crucial to preserve vital tissues, such as the sciatic nerve to preserve collateral damage. Preservation is particularly challenging when operating on body parts with complex tissue types, such as a femur, including hard and soft bone, muscle, fat and skin, and most importantly, the sciatic nerve.[4,5]

The sciatic nerve is the largest in the human body, measuring up to 2 cm in diameter. Originating from the lumbar and sacral spine, the sciatic nerve travels through the greater sciatic foramen below the piriformis muscle. Surrounded by a fatty sheath, it follows the upper thigh's back, from the pelvis to the knee. At the popliteal fossa, which serves as a conduit for blood vessels and nerves in the leg, the sciatic nerve divides into the common peroneal nerve and the tibial nerve. Both are responsible for motor and sensory function in the lower leg and foot.[6,7] Nerves are embedded in various other tissues, making it challenging for surgeons to discriminate between them, mostly smaller diameter nerves. Damaging the sciatic nerve's anatomical structure or the subsequent common peroneal and tibial nerves can drastically affect sensation over the sole, the back of the femur, part of the lower femur and the knee.[8–10] Fractional damage to the nerve can cause weakness of foot movements, weakness of knee flexion (bending), trouble bending the foot down (plantar flexion), or bending the foot inward (inversion).[11] Different approaches have already been proposed in the literature to detect nerves during laser ablation. For example, electrical stimulation, diffuse reflectance spectroscopy, optical spectroscopy, and mass spectroscopy have been proposed to detect the nerve tissue during laser ablation or surgery; however, no one has investigated it in a minimally invasive setting.[4,12]

Depending on the laser's parameters (i.e., pulse duration, wavelength, and output energy), superficial or deep ablation can occur with minimal temperature dissipation. In other words, when using lasers at a wavelength of 2940 nm, deep ablation can occur; this is not the case at 532 nm, where only superficial ablation is possible. To achieve deep ablation, different lasers have been compared and the results suggest that microsecond 2.94-μm Er:YAG (erbium-doped yttrium aluminum garnet) lasers can provide high ablation rate with high efficiency,[13,14] mainly because the operation wavelength of the Er:YAG laser corresponds to the highest absorption peak of water and hydroxyapatite, the main component of bone.[15,16] In contrast to the Er:YAG, the Nd:YAG (neodymium-doped yttrium aluminum garnet) laser source operating at 532 nm is transparent in water and seems well suited for tissue ablation in a liquid environment, such as knee arthroscopy.[15,17] Additionally, by using a nanosecond (ns) pulsed laser at 532 nm, we fulfill the thermal confinement condition in biological tissues. Therefore, a ns-pulsed Nd:YAG laser at 532 nm could be alternatively used to avoid thermal damage, producing superficial ablation.[17–19] Moreover, since the ablation rate is less than that of Er:YAG lasers, the risk of ablating more than one tissue at the same time is also less, leading to an in increase the possibility of preserving vital tissues.

Furthermore, when ns-pulsed lasers interact with biological tissues, acoustic shock waves (ASWs) from plasma-induced ablation are generated and can propagate through the air.[20] The propagated ASW can be measured using piezoelectric transducers, air-coupled transducers (microphones), and free-space Mach–Zehnder interferometer sensors, which convert the spherical wavefront into electrical signals.[21–24] ASW signal parameters mainly depend on the type of tissue ablated.[21] Therefore, feedback of these parameters can be used for real-time tissue differentiation.[24,25] The previously proposed bulky sensors to measure ASWs had limited bandwidths (typically <1 MHz) and were not suitable for minimally invasive setting.[26] The need for both a broad bandwidth and compact sensor led to new optical sensors, with extended bandwidths and small designs sufficient for endoscopic applications.[27] Interferometric-based methods detect variations in the optical interference patterns generated by the ASWs. Interference pattern variation is due to the ASW pressure that can interact directly with the interrogating beam, vary the resonance frequency, or cause reflector vibration. Depending on how the interferometer is configured, interference pattern variations are triggered by changes in the mean free path, the optical wavelength, or the optical phase.[24] The resulting variations in intensity or frequency of the interferometer output are measured by a photodiode and generate information about the ASW signals.[3,27]

Also, according to the literature reviews, support vector machine (SVM) and artificial neural network (ANN) are effective and practical solutions for biomedical signal recognition.[28–30] The ANN behavior mostly depends on weights and transfer function. The output of the transfer function is multiplied weights connecting the hidden layer and the output layer to generate the network output.[31] Consequently, in our previous study, we compared the performance of PCA combined with either a quadratic and Gaussian VMs or an ANN method.[32] The ANN was composed of a pattern network function combined with the Tan-Sigmoid activation function in the hidden layers. The main advantage of the Hyperbolic Tangent Function (Tanh) is that it generates a zero-centered output, thus strengthening the backpropagation process. The multilayer networks can use the Tan-Sigmoid function and the output neurons are often used for pattern recognition problems. Softmax activation function which was also known as a normalized exponential function was further employed to the output layer to predict the label.[33,34] Furthermore, ANN is a nonlinear model that is easy to use and understand compared to statistical methods, because ANNs are nonparametric models while most of the statistical methods are parametric models that need higher

background of statistics. That is why ANN with back-propagation learning algorithm is widely used in solving various classification and forecasting problems.[35,36] In addition, it has been found in our previous study that the ANN showed the best performance in terms of classifying all tissues during ablation.[3,32] Thus, ANN was also used for this optoacoustic data.

In this study, we used our custom-made fiber-coupled Fabry–Pérot etalon system to measure ASWs during laser ablation.[27] Among the advantages of using etalon sensors are their compactness and broad usable bandwidths (exceeding 2.5 MHz). We used a frequency-doubled, Q-switched Nd:YAG laser at 532 nm to produce craters on the surface of hard bone, soft bone, muscle, fat, skin, and nerve tissue. We measured the ASWs emitted and then assessed the measurements by looking at the frequency band that delivered the best accuracy and area under the curve (AUC). We used principal component analysis (PCA) and an ANN to reduce the dimensionality of data points and to classify sciatic nerve from among other tissue types, respectively.

MATERIALS AND METHODS

Sample preparation

In the experiments, we used samples from two fresh porcine proximal and distal femurs. Figures 1A–F and 1G–L show pictures of six tissue types (hard bone, soft bone, muscle, fat, skin, and nerve) which were obtained from porcine proximal and distal femurs, respectively. The connective tissues were carefully separated with scalpels. The samples were then rinsed in distilled water before undergoing the laser experiments.

Experimental setup

We ablated the samples using a Nd:YAG laser (Q-smart 450; Quantel) with 5 ns-long pulses at 532 nm. The pulse energy was 200 mJ, with a repetition frequency of 10 Hz. The laser beam was focused at a 7.5 cm focal distance (LA5042; Thorlabs), using an antireflection coated biconvex lens. A detailed explanation of the experimental setup, including calibration steps, was reported in previous work.[37] The focal point was positioned 2 mm under the sample surface to achieve deeper ablation. Using a Gaussian distribution, whereby maximum irradiance is reached at an amplitude of e^{-2}, the laser spot size was estimated to be 15.6 µm. A sequence of 180 laser pulses was applied to the fresh porcine femur. Ten craters, each 4 mm apart, were created on the surface of each sample.

In the optical sensor system, we used a single-frequency laser source (SFL1550S; Thorlabs) that emits continuous coherent light at a center wavelength of 1550 nm, with an output power of 40 mW. The laser contains a single-mode (SM) output fiber tail (CLD1015; Thorlabs). The output of the fiber tail is coupled into Port 1 (P1 in Figure 2) of the single-mode fiber-optic circulator (FOC) (6015-3-APC; Thorlabs). A single-mode 50:50 partial reflector fiber (P5- SMF28ER-50-1; Thorlabs) is connected to Port 2 (P2 in Figure 2) of the FOC to split the incident beam into two spectral bands: one transmitted and one reflected. The reflected light from the coated facet of the fiber is routed to Port 3 (P3). The transmitted light is collimated at the surface of an antireflection coated biconvex lens (67-593; Edmund Optics). The coated double-convex lens with a focal length of 9 mm is embedded in the 4 × 20 mm optical cavity to focus the collimated light onto the surface of a flat mirror. The propagating beam in the optical cavity is

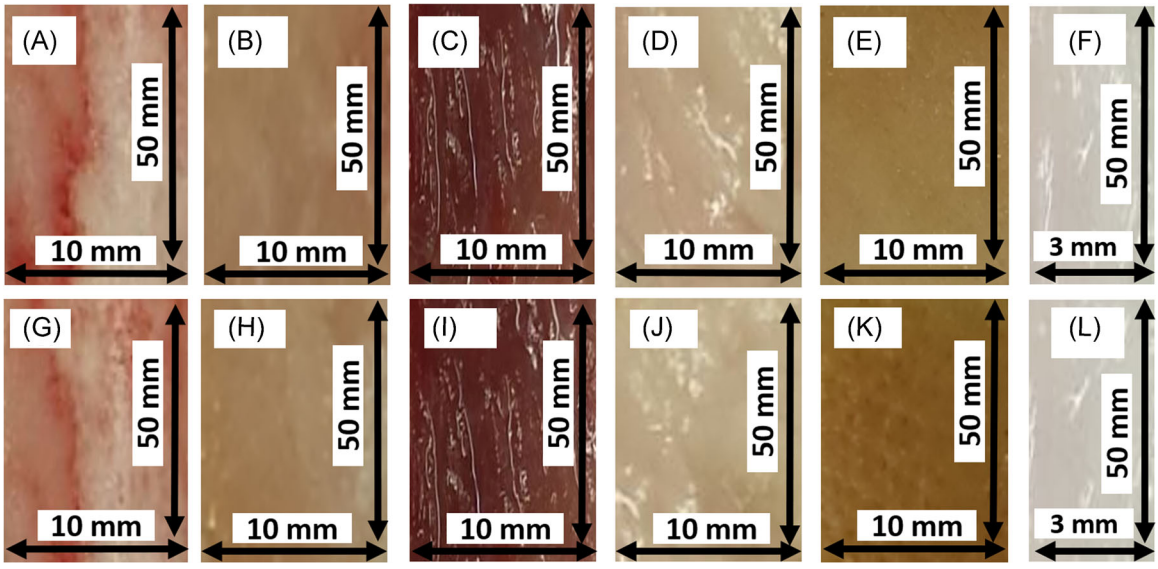

FIGURE 1 Tissue samples from a fresh porcine femur. Proximal femur: hard bone (A), soft bone (B), muscle (C), fat (D), skin (E), and nerve (F); distal femur: hard bone (G), soft bone (H), muscle (I), fat (J), skin (K), and sciatic nerve (L)

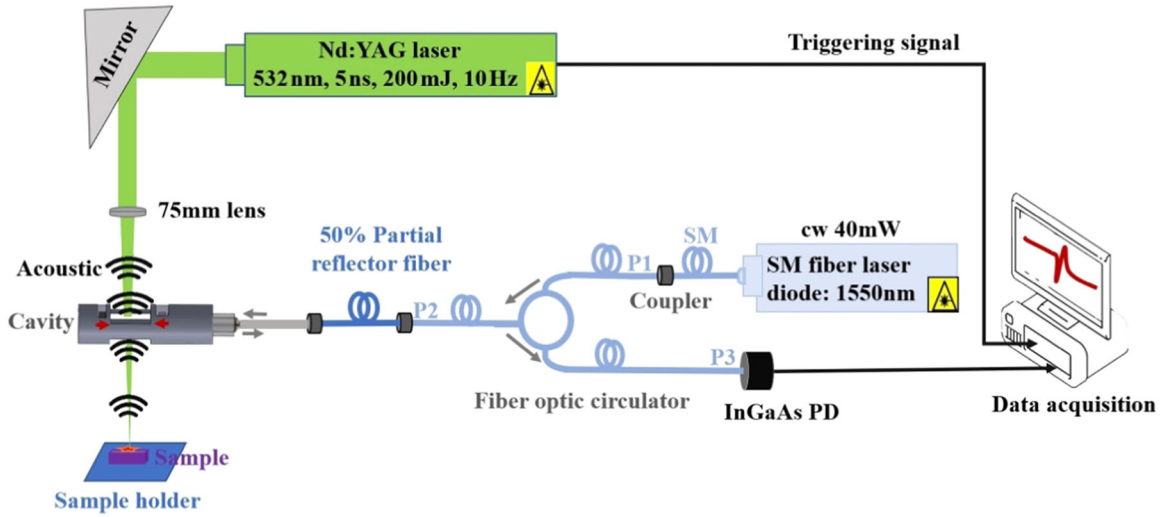

FIGURE 2 Illustration of the fiber-coupled Fabry–Pérot etalon system (side view). The acoustic shock wave propagated is detected in the optical cavity as the refractive index in the air cavity changes

retroreflected by a protected gold mirror (PF1011-M01; Thorlabs) and coupled back into the 50:50 partial reflector fiber. The FOC also routes the retroreflected beam to P3. The FOC's P3 connector is mounted to an InGaAs detector with a fixed amplifier gain (PDA20C2; Thorlabs) to sense the variation in light intensity.

During laser tissue ablation, the ASWs generated cause spatiotemporal variations of the air refractive index in the optical cavity. Thus, changes in the light intensity of the probing laser beam in the optical cavity correspond to the ASW pressure, which can be accurately measured by an InGaAs detector. The custom-made all-fiber Fabry–Pérot sensor is illustrated in Figure 2.

Data acquisition

During laser tissue ablation, we measured the ASWs emitted using the custom-made optical sensor (Figure 2). Acoustic data acquisition was triggered by an external CMOS trigger from the laser. The time gate window of each measurement was 82 μs. The measured analog signals were digitized using a PCI Express x8 (M4i.44xx-x8; Spectrum Microelectronic GmbH), with a 16-bit transient recorder and a sampling rate of 10 MS/s.

Classification matrix

Statistical analysis and calculations were performed with MATLAB (version R2018b). We suppressed each ASW signal's phase shift by characterizing the amplitude spectrum, using the fast Fourier transform. We improved the contrast of the visualization of each ASW using the logarithm of the amplitude spectrum. We split the amplitude spectrum into six equal frequency bands (F1–6). We normalized each frequency band value by subtracting the mean of all frequency bands measured to enhance classification performance. Therefore, a mean of zero was obtained for each frequency range. Each frequency band was used as an input for PCA, which was applied to reduce the dimensionality while maintaining the patterns and trends of the ASW field.[38] In other words, PCA decomposes the data by generating orthogonal and, thus, independent linear combinations of the variables known as principal components (PCs) or PCA scores.

To classify tissue, we investigated the post-processed acoustics by looking at the spectral band in which we achieved the best average classification accuracy and the area under the ROC curve for nerve detection. We combined PCA scores with an ANN to carry out the classification (Figure 3).

We used the *pattern network* function combined with the *Tan-Sigmoid activation function* for hidden layers and the *SoftMax activation function* for the output layer available in MATLAB. To build the network, we used an input, one hidden, and an output layer. The input layer was made of three neurons for the first three PCA scores. The single hidden layer and output layer were made of 10 neurons and 6 output neurons, respectively (Figure 4).

Only a few PCA scores are needed to describe the large variability of the data points. Thus, by using only three PCA scores, we were able to reduce the dimensionally of the frequency band while keeping most of the variance of the selected frequency band for classification (Figures 5 and 6A,B).

A total of 7200 ASWs were measured for each type of tissue extracted from two femurs—each femur has a proximal and a distal. During the classification phase, we used a set of 3600 data points measured from 10 craters in one proximal and distal femur as training data. During the validation phase, 1800 data points were used from the

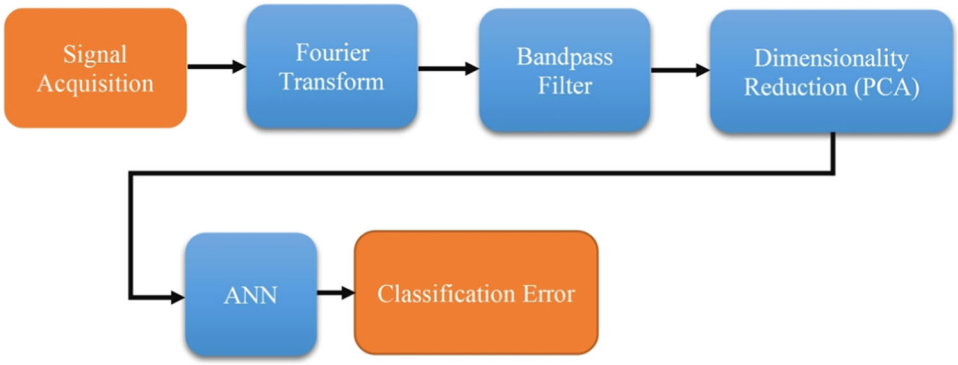

FIGURE 3 Flow chart of the signal processing methods for tissue classification

FIGURE 4 The architecture of our artificial neural network used to classify the first three principal component analysis scores of each acoustic shock wave from each tissue type

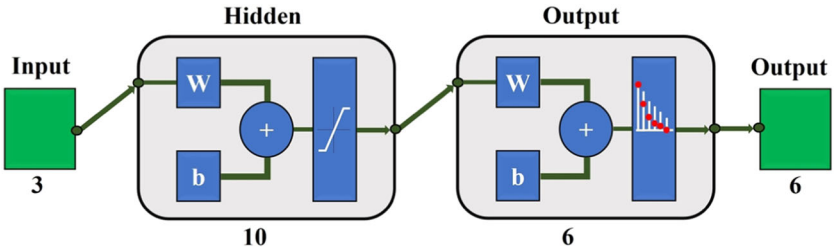

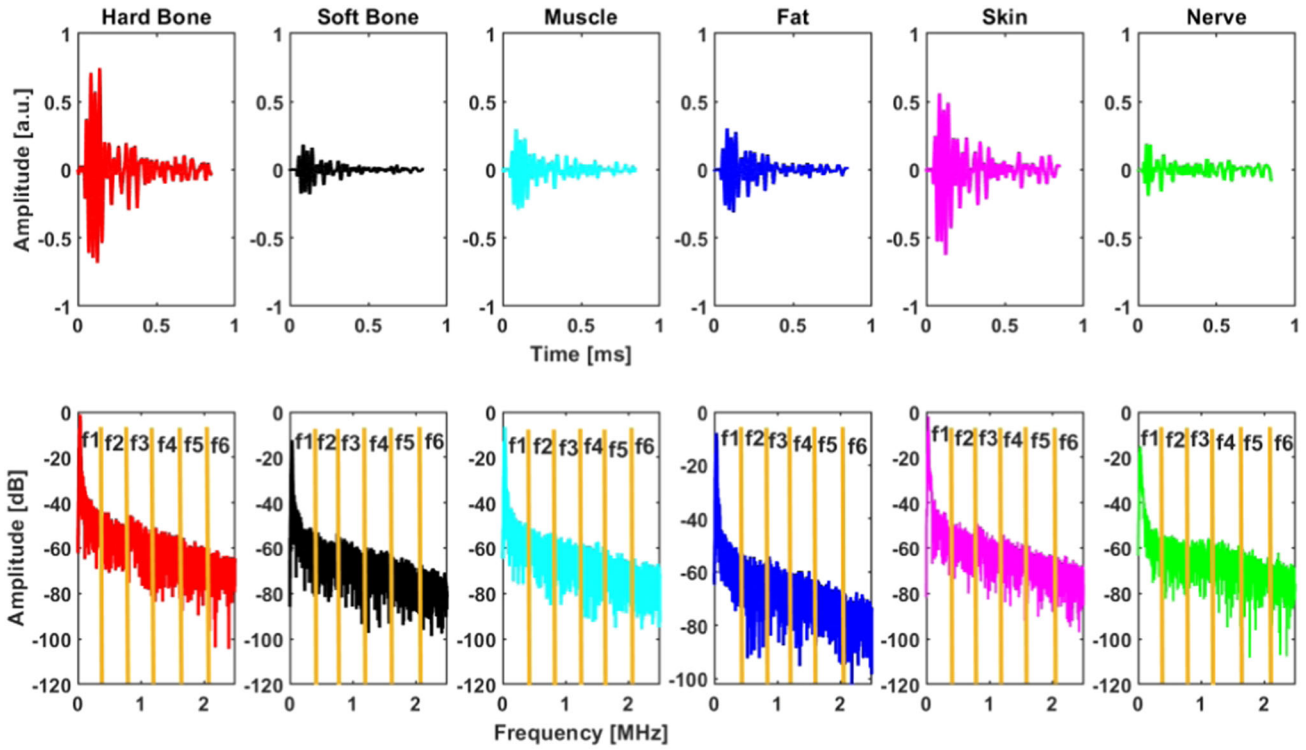

FIGURE 5 Comparison of the acoustic shock waves emitted from ablated hard muscle and fat tissues in the time and frequency domain

second proximal femur, and the remaining 1800 data points from the same femur were used as testing data. We performed a leave-one-out cross-validation by using the second femur as training data and the first one as validation and testing data. From the two confusion matrices and the receiver operating characteristics (ROCs), we calculated the mean accuracy of the testing-data-based scores for sciatic nerve classification and the AUC with a 95% confidence-level interval. We evaluated the performance of our models fairly on a single

computer with a specification of 2.4 GHz Intel Core i7 processor, 16 GB 1867 MHz DDR3 memory.

RESULTS

ASWs measured in the time and frequency domains for each ablated tissue are shown in Figure 5. Hard tissue (hard bone) produced higher peak amplitude values in the time and frequency domains than did the soft tissues (soft bone, muscle, fat, skin, and nerve). We used each frequency band as input for the PCA (see Appendix A for results at frequency bands, except for FR4).

The analysis of the training and testing data scores from frequency range FR4 are shown in Figures 6A and 6B, respectively. Results from other frequency bands are in Appendix A (Figures A1–A5 and Tables A1–A5). The first three PCs selected for differentiation were responsible for 87.5% of the variation around the data point where the first contributed 85.28% (PC1) followed by 1.89% (PC2) and 0.33% (PC3) to the cumulative variance. From the confusion matrix and the ROC analysis (Figure 4C), the average classification accuracy (with leave-one-out cross-validation) between nerve tissue and other tissues was more than 95.78 ± 1.3% (Table 1). The corresponding AUC was more than 99.58 ± 0.6%, for nerve, against other tissues (Table 1). Backpropagation was used for training with a learning rate of 2.4 ms. The computation time for testing was of the order of 0.46 ms.

DISCUSSION

Based on the confusion matrix and the ROC analysis of the model's tissue classification results, nerve tissue could be classified with an accuracy rate and AUC results of

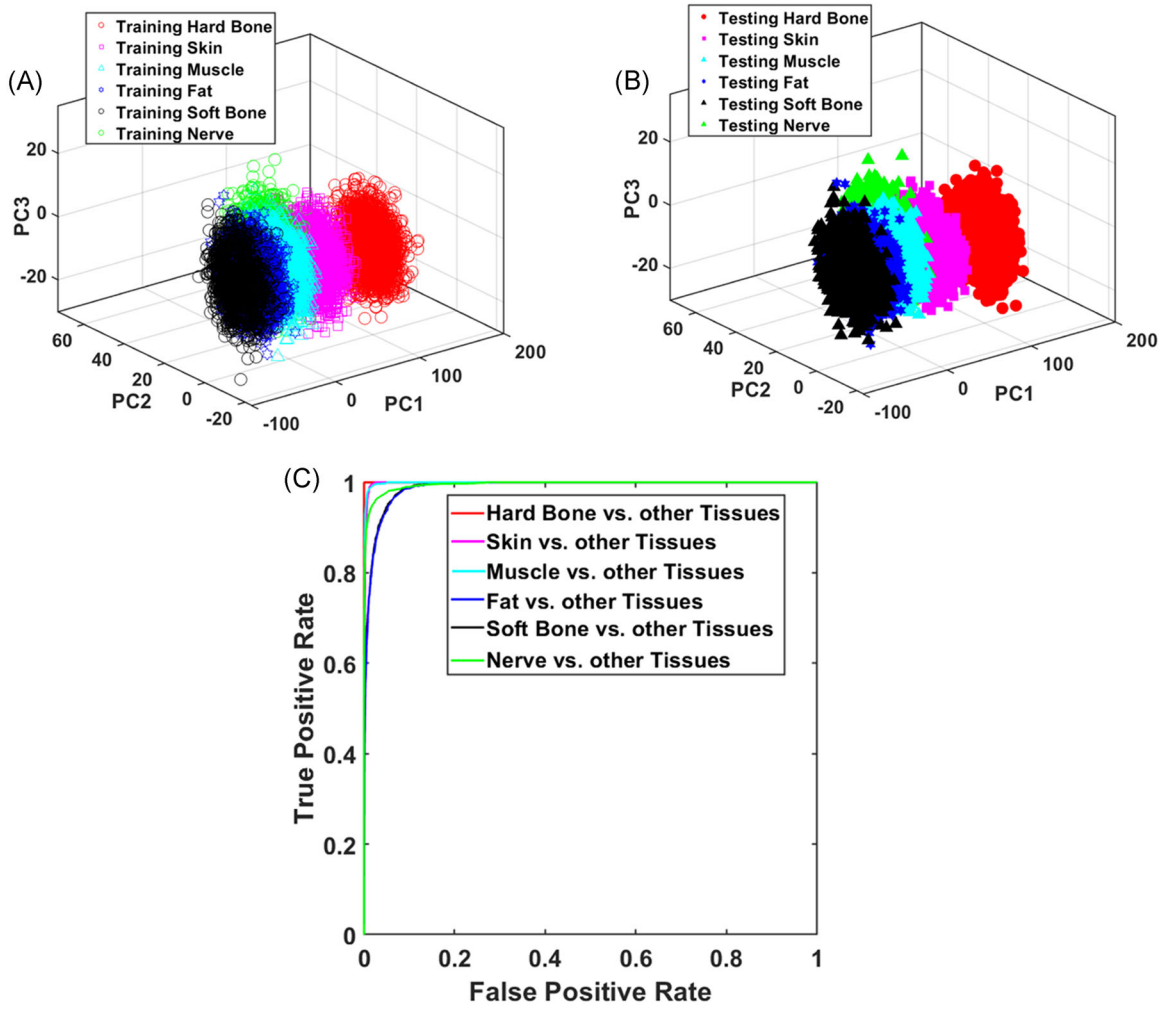

FIGURE 6 First three principal component (PC) scores from (A) the training data for hard and soft bone, muscle, fat, skin, and nerve (FR4 = 1.25–1.67 MHz), using the artificial neural network (ANN) models combined with the nanosecond (ns)-Nd:YAG laser. First three PC scores from (B) the testing data for hard and soft bone, muscle, fat, skin, and nerve (FR4 = 1.25–1.67 MHz), using the ANN models combined with the ns-Nd:YAG laser. The receiver operating characteristic curve (C) to multiclass using the ANN models combined with the ns-Nd:YAG laser. Note that the curve of hard bone, skin, muscle, and nerve tissues versus other tissues overlaps

TABLE 1 Confusion matrix for hard bone, skin, muscle, fat, soft bone, and nerve tissues (FR4 = 1.25–1.67 MHz) during laser ablation at 0.2 J pulse energy

	Classified as							
Tissue	**Hard bone**	**Skin**	**Muscle**	**Fat**	**Soft bone**	**Nerve**	**Average classification accuracy with leave-one-out cross-validation (%)**	**Area under ROC curve (%)**
Hard bone	1800	0	0	0	0	0	100	100
Skin	0	1734	0	0	0	66	99.33	99.91
Muscle	0	0	1712	7	0	81	95.11	99.83
Fat	0	0	9	1593	198	0	88.50	98.90
Soft bone	0	0	0	198	1602	0	89	98.98
Nerve	0	43	33	0	0	1724	95.78	99.58

Abbreviation: ROC, receiver operating characteristic.

95.78 ± 1.3% and 99.58 ± 0.6%, respectively. With an accuracy rate and AUC of 100%, the best result was achieved for distinguishing hard bone tissue from all others. The main reason for this high classification rate is that hard tissues, like hard bone, consist of 65% inorganic elements (calcium phosphate compounds, mainly hydroxyapatite) and 35% organic elements (collagen fibrils, water, proteins). In contrast, soft tissue is 79% water, which is its main chromophore, and 20% pigment melanin, lipids, and carbohydrates.[39] In other words, the ASWs that emanate from soft tissues are mainly generated by water, while those that originate from hard bone are mostly based on carbonated hydroxyapatite.[32,40] The worst classification rate and AUC results were for distinguishing between soft bone and fat (Tables A1–A5). This tendency for misclassification was already observed in our earlier studies.[24,27] Since soft bone in the femur is mostly made of fatty tissue, it presents a similar mechanical structure, generating comparable ASW signatures.[24,27] Nevertheless, classification between tissue types was not the main aim of this study, in which we focused on sciatic nerve at a frequency range of 1.25–1.67 MHz (FR4). The frequency bands were chosen ad hoc, however, by further reducing the size of the frequency band, we observed less accuracy. Therefore, the best results were obtained by splitting the amplitude spectrum into six equal frequency bands. In our previous studies, we showed that the frequency band of 1.67–2.08 MHz (FR5) yielded the best results in terms of high average classification accuracy and AUCs with cross-validation between tissues.[24,27,41] The higher values were theoretically expected, as the ablation with the Nd:YAG is based on plasma mediation, which increases the pressure energy measured by the optical sensor. The authors believe by adding nerve tissues the frequency range that provided the best classification accuracy shifted to 1.25–1.67 MHz (FR4). The main reason could be the important parameters (variance) of the ASWs from nerve are in the frequency range of FR4. Additionally, the PCA was used to reduce the data dimensionally at each frequency range. This is because PCs consecutively maximize variance and can be obtained from the eigenvalues/eigenvectors of a covariance matrix.[42] When all variables are measured in the same units, covariance-based PCA may be suitable. In general, the first PCs are dominated by the high-variance variables and mostly represent variance of each data. Therefore, by confining the number of eigenvalues and eigenvectors to the first three PCs, we aim to keep the most represented variance of each data and improve the speed of online classifier when transferring feedback sensor to other systems for in-vivo measurements. In case the online classifier produces more errors, more PCs can be used to address this issue, however, the computational time would increase.[32]

To apply this tissue classification method in a closed-loop system to control laser ablation in surgery, the computational time needed to analyze the ASW spectra must be less than the pulse repetition time. To extend the system for a more general purpose, it would be essential to analyze numerous types of tissue in a very short period of time; an aim that presents both a mathematical and computational challenge. While determining the computational time for tissue classification was not the objective of our study, the matter must be examined further before transferring the investigation results to a control system. In our study, tissue classification was implemented ex vivo. Before any clinical use of the model, however, additional tests would be required to examine the impact of blood flow in vivo and carbonization on the surface of surgical lesions on ASW tissue classification.

The method still needs to be improved. It could be improved by using deep learning to further reduce the error rate. We can also use a filter to leave out misclassified data, that is, when doing line cut on top of hard bone with laser, we detect hard bone during the last five shots. Unexpectedly, we detect muscle in one shot followed by the detection of soft bone. The software will just filter out the misclassified skin and considers it as outlier or hard bone.

As already mentioned, the Er:YAG laser at 2940 nm is generally used for deep ablation accompanied by a water-cooling system,[15] while, the Nd:YAG laser at 532 nm can be used to ablate surfaces in a wet environment.[20,25,43] Depending on the laser pulse parameters, such as laser energy, pulse duration, and focusing conditions,[43] the ASW properties can be slightly different.[20] Therefore, for more application, investigating tissue classification using the Er:YAG at 2940 nm combined with the Nd:YAG laser at 532 nm in vivo is an essential next step.

CONCLUSION

The results of this study show the potential of using ASW for remote classification of nerve and other types of tissue (hard and soft bone, muscle, fat, and skin). The average classification accuracy and AUC result with leave-one-out cross-validation was more than 95.78 ± 1.3% for distinguishing nerves from other tissues. This technology can be used to develop a control system capable of identifying nerve tissue during endoscopic laser surgery to prevent sensation and motor function loss in the lower body. Future work should focus on tissue classification and carbonization detection with sufficiently short computational time when ablating a wide range of tissue types in vivo, using Nd:YAG and Er:YAG at 532 and 2940 nm, respectively.

ACKNOWLEDGMENT

This project is part of the MIRACLE (Minimally Invasive Robot-Assisted Computer-guided Laser-osteotomE) project funded by the Werner Siemens Foundation. Open access funding provided by Universitat Basel.

CONFLICT OF INTERESTS

The authors declare that there are no conflict of interests.

ORCID

Hervé Nguendon Kenhagho https://orcid.org/0000-0002-6364-3180

REFERENCES

1. Kuttenberger JJ, Stübinger S, Waibel A, Werner M, Klasing M, Ivanenko M, et al. Computer-guided CO_2-laser osteotomy of the sheep tibia: technical prerequisites and first results. Photomed Laser Surg. 2008;26(2):129–36.
2. Stopp, S, Svejdar D, Kienlin Ev, Deppe H, Lueth TC. A new approach for creating defined geometries by navigated laser ablation based on volumetric 3-D data. IEEE Trans Biomed Eng. 2008;55(7):1872–80. https://doi.org/10.1109/TBME.2008.919737
3. Kenhagho HN, Canbaz F, Guzman R, Cattin P, Zam A. Miniaturized optoacoustic feedback sensor for smart laser osteotome: fiber-coupled Fabry-Pérot etalon sensor. Sens Actuators, A. 2020;317:112394. https://doi.org/10.1016/j.sna.2020.112394
4. Stelzle F, Zam A, Adler W, Tangermann-Gerk K, Douplik A, Nkenke E, et al. Optical nerve detection by diffuse reflectance spectroscopy for feedback controlled oral and maxillofacial laser surgery. J Transl Med. 2011;9(1):20. https://doi.org/10.1186/1479-5876-9-20
5. Baxter G, Walsh D, Allen J, Lowe A, Bell A. Effects of low intensity infrared laser irradiation upon conduction in the human median nerve in vivo. Exp Physiol. 1994;79(2):227–34. https://doi.org/10.1113/expphysiol.1994.sp003755
6. Valat J-P, Genevay S, Marty M, Rozenberg S, Koes B. Sciatica. Best Pract Res Clin Rheumatol. 2010;24:241–52. https://doi.org/10.1016/j.berh.2009.11.005
7. Darras BT, Jones HR, Darryl C, editors. Neuromuscular disorders of infancy, childhood, and adolescence: a clinician's approach. Elsevier; 2014.
8. Menovsky T, van den Bergh Weerman M, Beek JF. Effect of CO_2 milliwatt laser on peripheral nerves: Part I. A dose-response study. Microsurgery. 1996;17(10):562–67. https://doi.org/10.1002/(sici)1098-2752(1996)17:10<562::Aid-micr6>3.0.Co;2-s
9. Inserra MM, Bloch DA, Terris DJ. Functional indices for sciatic, peroneal, and posterior tibial nerve lesions in the mouse. Microsurgery. 1998;18(2):119–24.
10. Burkhart FL, Daly JW. Sciatic and peroneal nerve injury: a complication of vaginal operations. Obstet Gynecol. 1966;28(1):99–102.
11. Abitbol J, Gendron D, Laurin C, Beaulieu M. Gluteal nerve damage following total hip arthroplasty: a prospective analysis. J Arthroplasty. 1990;5(4):319–22.
12. Garcia-Losarcos N, Gonzalez-Hidalgo M, Franco-Carcedo C, Poch-Broto J. Estimulacion electrica del nervio facial con funcion pronostica en la cirugia de parotida [Electrical stimulation of the facial nerve with a prognostic function in parotid surgery]. Rev Neurol. 2009;49(3):119–22.
13. Peavy GM, Reinisch L, Payne JT, Venugopalan V. Comparison of cortical bone ablations by using infrared laser wavelengths 2.9 to 9.2 μm. Lasers Surg Med. 1999;25(5):421–34.
14. Walsh JT, Jr., Deutsch TF. Er:YAG laser ablation of tissue: measurement of ablation rates. Lasers Surg Med. 1989;9(4):327–37.
15. Kuscer L, Diaci J. Measurements of erbium laser-ablation efficiency in hard dental tissues under different water cooling conditions. J Biomed Opt. 2013;18:108002.
16. Fekrazad R, Kalhori K, Ahrari F, Nikoo T. Laser in orthodontics. INTECH Open Access Publisher; 2011.
17. Tulea C-A, Caron J, Gehlich N, Lenenbach A, Noll R, Loosen P. Laser cutting of bone tissue under bulk water with a pulsed ps-laser at 532 nm. J Biomed Opt. 2015;20:105007.
18. Oosterbeek RN, Ward T, Ashforth S, Bodley O, Rodda AE, Simpson MC. Fast femtosecond laser ablation for efficient cutting of sintered alumina substrates. Opt Lasers Eng. 2016;84:105–10. https://doi.org/10.1016/j.optlaseng.2016.04.007
19. Ashforth SA, Simpson MC, Bodley O, Oosterbeek R. *Ultrashort pulse laser interactions with cortical bone tissue for applications in orthopaedic surgery* (SPIE LASE). SPIE; 2015.
20. Kenhagho HN, Rauter G, Guzman R, Cattin PC, Zam A. *Comparison of acoustic shock waves generated by micro and nanosecond lasers for a smart laser surgery system, in SPIE BiOS*. Vol. 10484. SPIE; 2018. p. 9.
21. Nguendon HK Faivre N, Meylan B, Shevchik B, Rauter G, Guzman R, et al. Characterization of ablated porcine bone and muscle using laser-induced acoustic wave method for tissue differentiation, in Medical Laser Applications and Laser-Tissue Interactions. Vol. 10417. SPIE Proceedings (Optical Society of America, 2017).
22. Brecht H-P. F, Su R, Fronheiser M. P, Ermilov S. A, Conjusteau A, Oraevsky A. A. Whole-body three-dimensional optoacoustic tomography system for small animals. J Biomed Opt. 2009;14(6):1–8. https://doi.org/10.1117/1.3259361
23. Fehm TF, Deán-Ben XL, Razansky D. Four dimensional hybrid ultrasound and optoacoustic imaging via passive element optical

excitation in a hand-held probe. Appl Phys Lett. 2014;105(17): 173505.
24. Kenhagho HN, Rauter G, Guzman R, Cattin P, Zam A. Optoacoustic tissue differentiation using a Mach-Zehnder interferometer. IEEE Trans Ultrason Eng. 2019;66:1435–43. https://doi.org/10.1109/TUFFC.2019.2923696
25. Nguendon Kenhagho K, Shevchik S, Saeidi F, Faivre N, Meylan B, Rauter G, et al. Characterization of abated bone and muscle for long-pulsed laser ablation in dry and wet conditions. Materials. 2019;12(8):1338. http://www.mdpi.com/1996-1944/12/8/1338
26. Yuldashev P, Karzova M, Khokhlova V, Ollivier S, Blanc-Benon P. Mach-Zehnder interferometry method for acoustic shock wave measurements in air and broadband calibration of microphones. J Acoust Soc Am. 2015;137(6):3314–24. https://doi.org/10.1121/1.4921549
27. Kenhagho HN, Canbaz F, Rauter G, Guzman R, Cattin P, Zam A. A first approach to miniaturized optoacoustic feedback sensor for smart laser osteotome: fiber-coupled Fabry-Pérot etalon sensor. 2019 IEEE Sens. 2019;2019:1–4. https://doi.org/10.1109/SENSORS43011.2019.8956743
28. Dehmeshki J, Chen J, Casique MV, Karakoy M, Classification of lung data by sampling and support vector machine, in *The 26th Annual International Conference of the IEEE Engineering in Medicine and Biology Society*, Sept. 1–5, 2004, Vol. 2, p. 3194–7. https://doi.org/10.1109/IEMBS.2004.1403900
29. Mehta SS, Lingayat NS, Biomedical signal processing using SVM, in *2007 IET-UK International Conference on Information and Communication Technology in Electrical Sciences (ICTES 2007)*, Dec. 20–22, 2007, p. 527–32.
30. Guenther FH. Neural networks: biological models and applications. In: Smelser NJ, Baltes PB, editors. International encyclopedia of the social & behavioral sciences. Oxford: Pergamon; 2001. p. 10534–37.
31. Gaopale K, Jamisola RS, Seitshiro I. Airblast prediction in a blasting operation using artificial intelligence. 2019.
32. Nguendon Kenhagho H, Canbaz F, Gomez Alvarez-Arenas TE, Guzman R, Cattin P, Zam A. Machine learning-based optoacoustic tissue classification method for laser osteotomes using an air-coupled transducer. Lasers Surg Med. 53:377–89. https://doi.org/10.1002/lsm.23290
33. Svensén M, Bishop CM. Pattern recognition and machine learning. 2007. https://scholar.google.fr/scholar?hl=de&as_sdt=0%2C5&as_vis=1&q=Pattern+recognition+and+machine+learning%2C+Bishop%2C+2006&btnG=
34. Lehman J, Risi S, Clune J. Creative generation of 3D objects with deep learning and innovation engines, in *Proceedings of the 7th International Conference on Computational Creativity*, 2016.
35. Andrearczyk V, Whelan PF. Deep learning in texture analysis and its application to tissue image classification. In: Depeursinge A, Al-Kadi OS, Mitchell JR, editors. Biomedical texture analysis. Academic Press; 2017. p. 95–129. https://scholar.google.fr/scholar?hl=de&as_sdt=0%2C5&as_vis=1&q=Deep+learning+in+texture+analysis+and+its+application+to+tissue+image+classification&btnG=
36. Alperovich Z, Yamin G, Elul E, Bialolenker G, Ishaaya AA. In situ tissue classification during laser ablation using acoustic signals. J Biophotonics. 2019;12:e201800405.
37. Kenhagho HN, Canbaz F, Guzman R, Cattin P, Zam A. Miniaturized optoacoustic feedback sensor for smart laser osteotome: fiber-coupled Fabry-Pérot etalon sensor. Sens and Actu A: Phys. 2020;317:112394.
38. Lever J, Krzywinski M, Altman N. Principal component analysis. Nat Methods. 2017;14:641–2. https://doi.org/10.1038/nmeth.4346
39. Curzon M, Featherstone J. Chemical composition of enamel. In: Lazzan EP, editor. Handbook of experimental aspects of oral biochemistry. Boca Raton, FL: CRC Press; 1983. p. 123–35.
40. Apel C, Meister J, Ioana R, Franzen R, Hering P, Gutknecht N. The ablation threshold of Er:YAG and Er:YSGG laser radiation in dental enamel. Lasers Med Sci. 2002;17(4):246–52.
41. Kenhagho HN, Rauter G, Guzman R, Cattin P, Zam A. Optoacoustic tissue differentiation using a Mach-Zehnder interferometer: preliminary results. in 2018 IEEE International Ultrasonics Symposium (IUS). 2018;2018:1–9. https://doi.org/10.1109/ULTSYM.2018.8579654
42. Jolliffe IT, Cadima J. Principal component analysis: a review and recent developments. Philos Trans R Soc A. 2016;374(2065): 20150202.
43. Manikanta E, Vinoth Kumar L, Venkateshwarlu P, Leela C, Kiran PP. Effect of pulse duration on the acoustic frequency emissions during the laser-induced breakdown of atmospheric air. Appl Opt. 2016;55(3):548–55. https://doi.org/10.1364/AO.55.000548

How to cite this article: Nguendon Kenhagho H, Canbaz F, Hopf A, Guzman R, Cattin P, Zam A. Toward optoacoustic sciatic nerve detection using an all-fiber interferometric-based sensor for endoscopic smart laser surgery. Lasers Surg Med. 2022;54:289–304.
https://doi.org/10.1002/lsm.23473

APPENDIX A

Tables A1–A5

Figures A1–A5

TABLE A1 Confusion matrix for hard bone, skin, muscle, fat, soft bone, and nerve tissues (FR1 = 0–0.42 MHz) during laser ablation at 0.2 J pulse energy

	Classified as						Average classification accuracy with leave-one-out cross-validation (%)	Area under ROC curve (%)
Tissue	Hard bone	Skin	Muscle	Fat	Soft bone	Nerve		
Hard bone	1798	2	0	0	0	0	99.88	100
Skin	0	1800	0	0	0	0	100	100
Muscle	0	0	1797	3	0	0	99.83	100
Fat	0	0	321	1479	0	0	82.17	98.65
Soft bone	0	0	0	259	1541	0	85.61	98.66
Nerve	0	0	0	0	0	1800	100	100

Abbreviation: ROC, receiver operating characteristic.

TABLE A2 Confusion matrix for hard bone, skin, muscle, fat, soft bone, and nerve tissues (FR2 = 0.42–0.83 MHz) during laser ablation at 0.2 J pulse energy

	Classified as						Average classification accuracy with leave-one-out cross-validation (%)	Area under ROC curve (%)
Tissue	Hard bone	Skin	Muscle	Fat	Soft bone	Nerve		
Hard bone	1799	1	0	0	0	0	99.94	100
Skin	0	1799	0	0	1	0	99.94	100
Muscle	0	0	1797	3	0	0	99.61	99.95
Fat	0	0	6	1475	185	134	81.94	97.37
Soft bone	0	0	0	214	1448	138	80.44	97.42
Nerve	0	0	14	165	192	1429	79.39	97.72

Abbreviation: ROC, receiver operating characteristic.

TABLE A3 Confusion matrix for hard bone, skin, muscle, fat, soft bone, and nerve tissues (FR3 = 0.83–1.25 MHz) during laser ablation at 0.2 J pulse energy

	Classified as						Average classification accuracy with leave-one-out cross-validation (%)	Area under ROC curve (%)
Tissue	Hard bone	Skin	Muscle	Fat	Soft bone	Nerve		
Hard bone	1800	0	0	0	0	0	100	100
Skin	1	1797	1	0	0	1	99.83	100
Muscle	0	1	1757	9	0	33	99.61	99.95
Fat	0	0	4	1582	207	7	87.89	98.68
Soft bone	0	0	0	114	1686	0	99.66	98.85
Nerve	0	0	135	7	0	1658	92.11	99.67

Abbreviation: ROC, receiver operating characteristic.

TABLE A4 Confusion matrix for hard bone, skin, muscle, fat, soft bone, and nerve tissues (FR5 = 1.67–2.08 MHz) during laser ablation at 0.2 J pulse energy

	Classified as							
Tissue	**Hard bone**	**Skin**	**Muscle**	**Fat**	**Soft bone**	**Nerve**	**Average classification accuracy with leave-one-out cross-validation (%)**	**Area under ROC curve (%)**
Hard bone	1796	4	0	0	0	0	99.78	100
Skin	0	1625	0	0	0	175	90.28	99.44
Muscle	0	0	1706	7	0	87	94.78	99.80
Fat	0	0	4	1585	210	1	88.06	98.84
Soft bone	0	0	0	267	1533	0	85.17	98.92
Nerve	0	104	27	0	0	1669	92.72	98.66

Abbreviation: ROC, receiver operating characteristic.

TABLE A5 Confusion matrix for hard bone, skin, muscle, fat, soft bone, and nerve tissues (FR6 = 2.08–2.50 MHz) during laser ablation at 0.2 J pulse energy

	Classified as							
Tissue	**Hard bone**	**Skin**	**Muscle**	**Fat**	**Soft bone**	**Nerve**	**Average classification accuracy with leave-one-out cross-validation (%)**	**Area under ROC curve (%)**
Hard bone	1788	4	0	0	0	8	99.33	100
Skin	0	1501	0	0	0	299	83.39	99.41
Muscle	0	0	1553	0	0	247	86.40	99.16
Fat	0	0	3	1520	227	50	84	98.35
Soft bone	0	0	0	267	1515	18	84.17	98.78
Nerve	3	105	64	13	0	1615	89.72	98.53

Abbreviation: ROC, receiver operating characteristic.

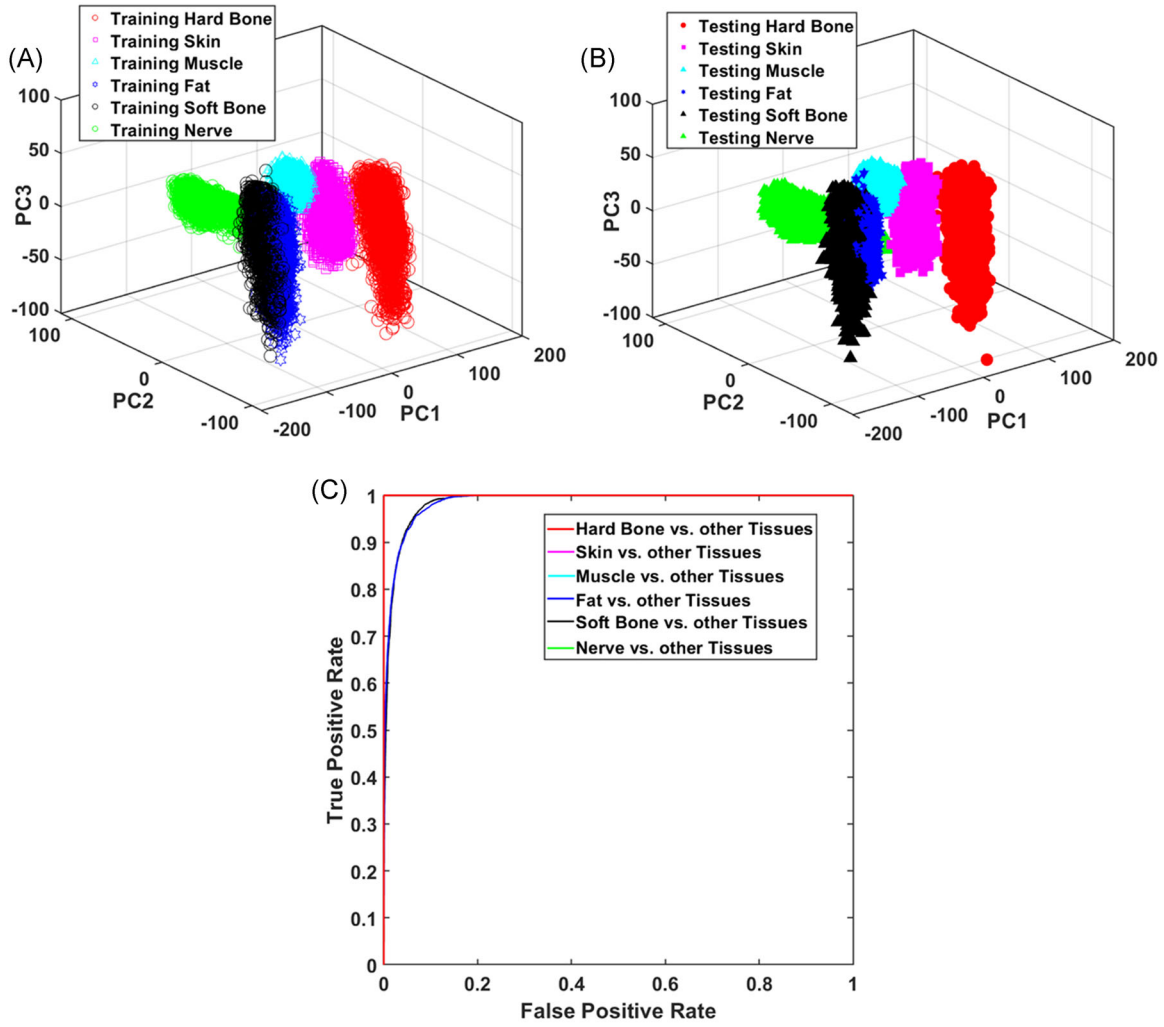

FIGURE A1 First three principal component (PC) scores from (A) the training data for hard and soft bone, muscle, fat, and skin (FR1 = 0–0.42 MHz). First three PC scores from (B) the testing data for hard and soft bone, muscle, fat, and skin (FR1 = 0–0.42 MHz). Receiver operating characteristic curve (C) to multiclass using the artificial neural network models combined with the ns-Nd:YAG laser. Note that the curve of hard bone, skin, muscle, and nerve tissues versus other tissues overlaps (FR1 = 0–0.42 MHz)

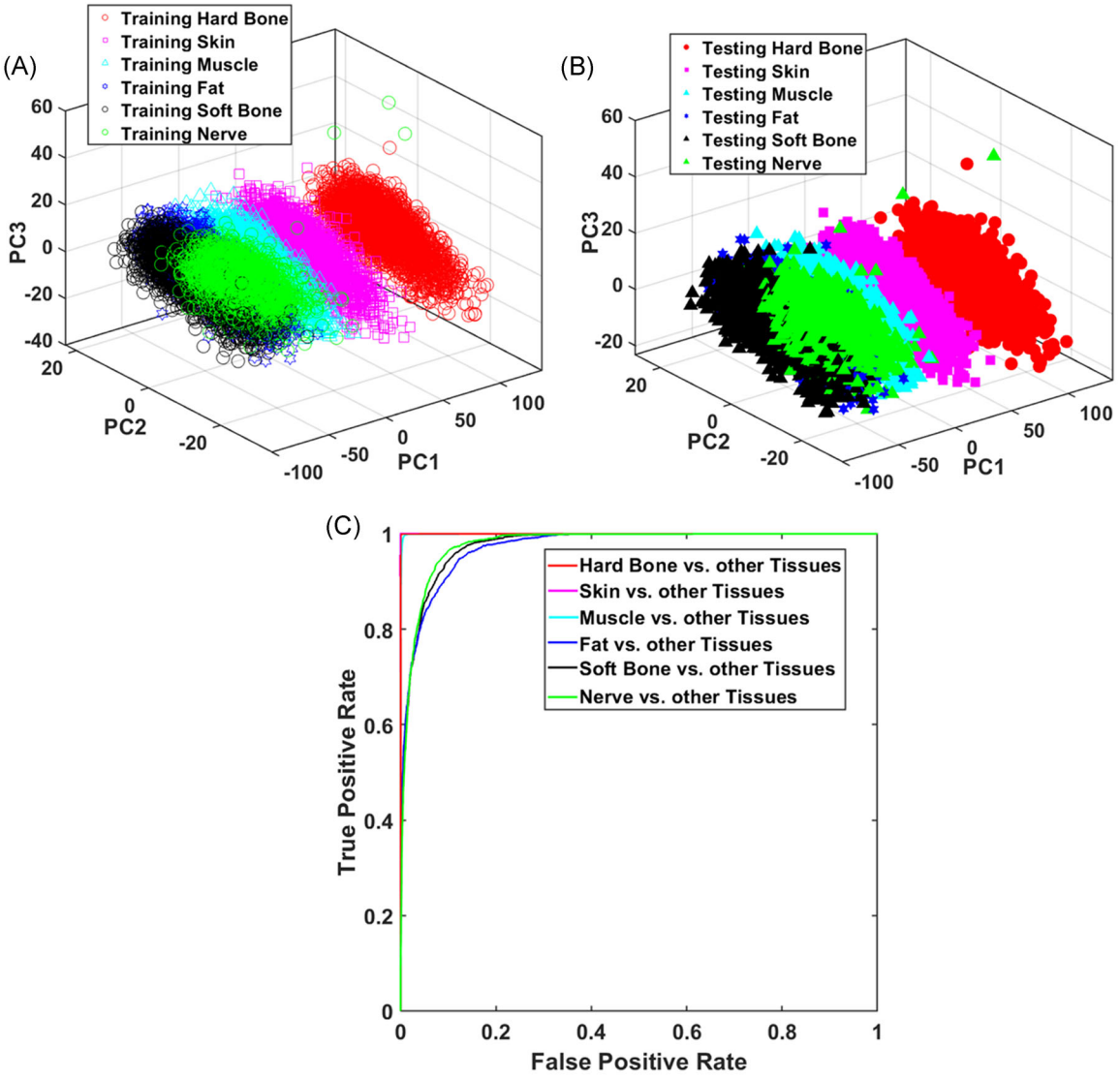

FIGURE A2 First three principal component (PC) scores from (A) the training data for hard and soft bone, muscle, fat, and skin (FR2 = 0.42–0.83 MHz). First three PC scores from (B) the testing data for hard and soft bone, muscle, fat, and skin (FR2 = 0.42–0.83 MHz). Receiver operating characteristic curve (C) to multiclass using the artificial neural network models combined with the ns-Nd:YAG laser. Note that the curve of hard bone, skin, muscle, and nerve tissues versus other tissues overlaps (FR2 = 0.42–0.83 MHz)

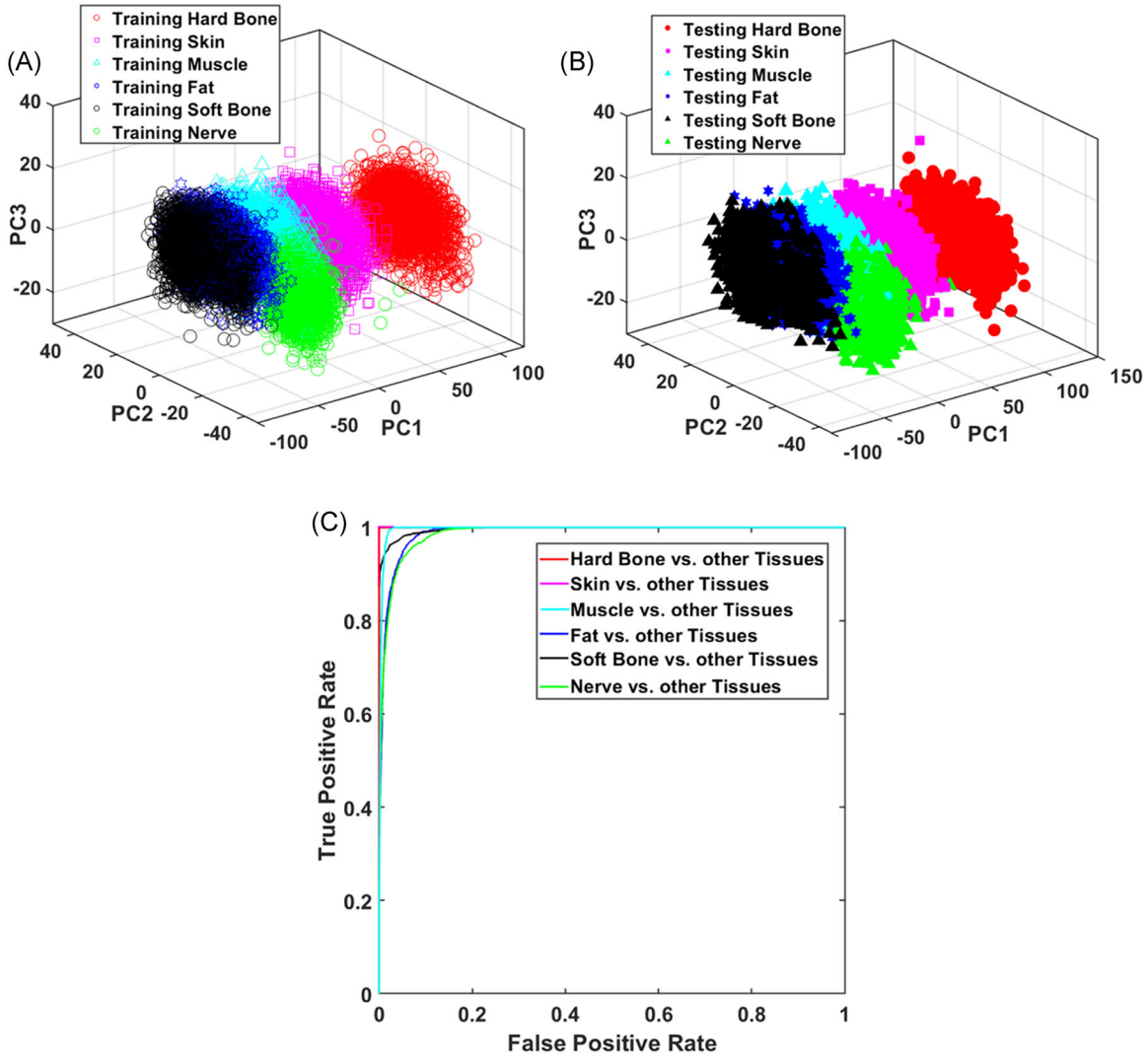

FIGURE A3 First three principal component (PC) scores from (A) the training data for hard and soft bone, muscle, fat, and skin (FR3 = 0.83–1.25 MHz). First three PC scores from (B) the testing data for hard and soft bone, muscle, fat, and skin (FR3 = 0.83–1.25 MHz). Receiver operating characteristic curve (C) to multiclass using the artificial neural network models combined with the ns-Nd:YAG laser. Note that the curve of hard bone, skin, muscle, and nerve tissues versus other tissues overlaps (FR3 = 0.83–1.25 MHz)

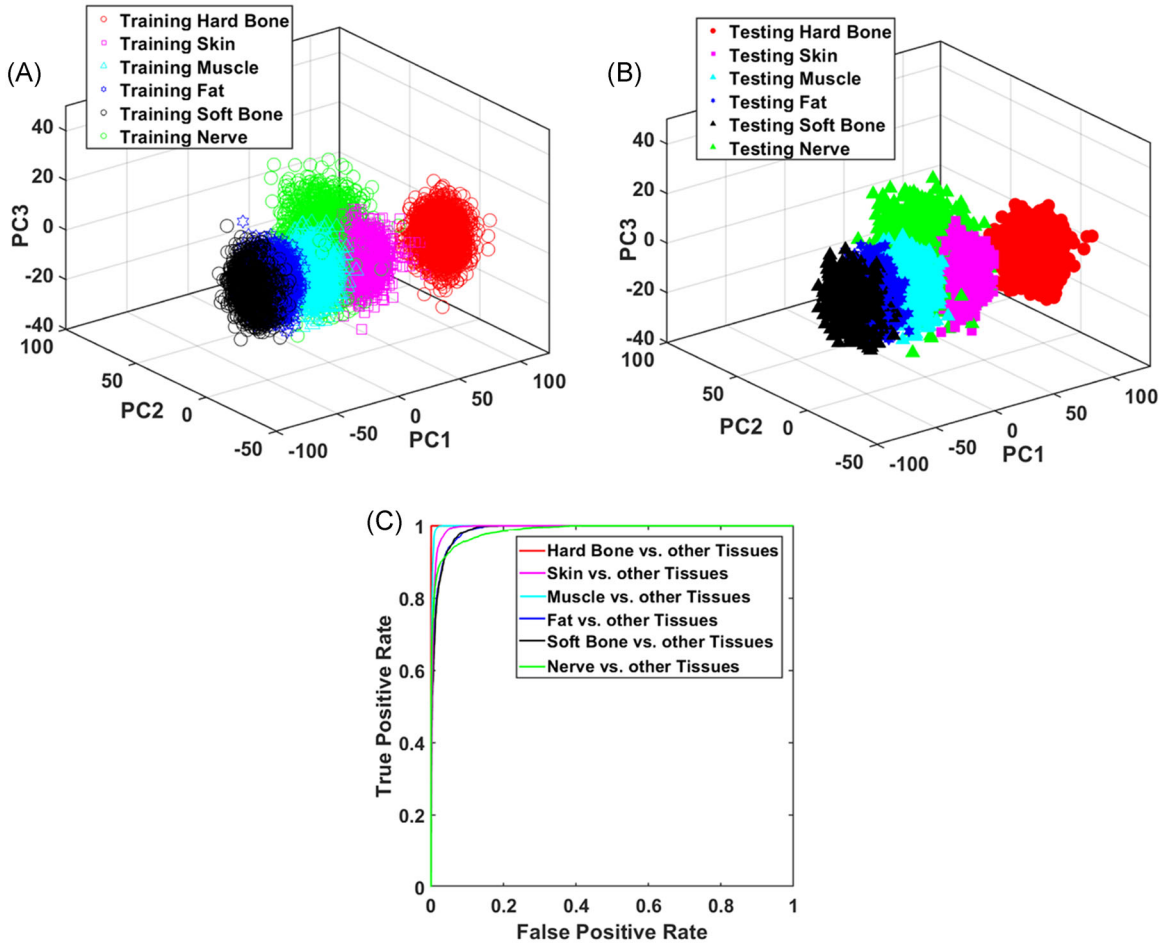

FIGURE A4 First three principal component (PC) scores from (A) the training data for hard bone, soft bone, muscle, fat, skin, and nerve (FR5 = 1.67–2.08 MHz). First three PC scores from (B) the testing data for hard bone, soft bone, muscle, fat, skin, and nerve (FR5 = 1.67–2.08 MHz). Receiver operating characteristic curve (C) to multiclass using the artificial neural network models combined with the ns-Nd:YAG laser. Note that the curve of hard bone, skin, muscle, and nerve tissues versus other tissues overlaps (FR5 = 1.67–2.08 MHz)

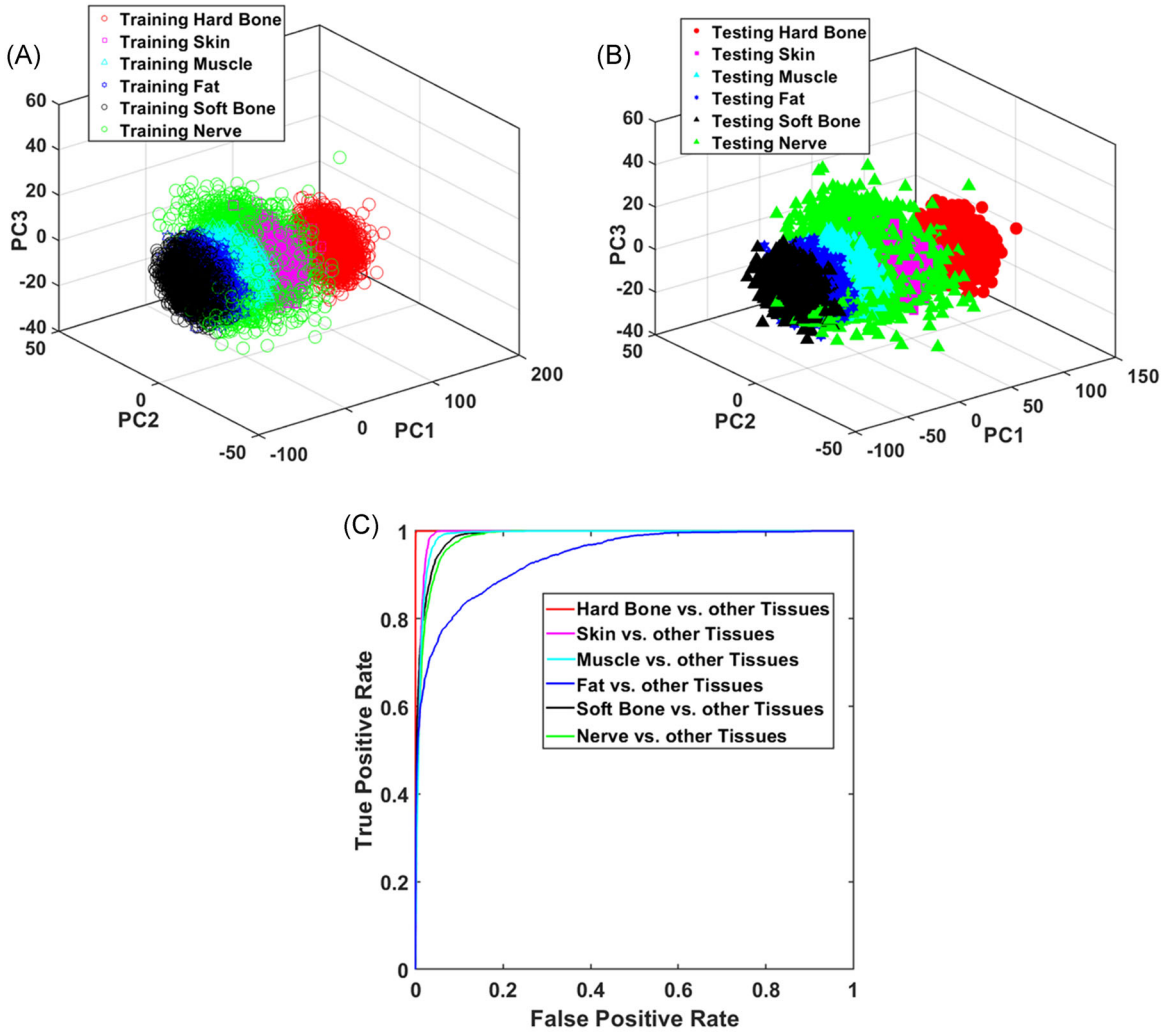

FIGURE A5 First three principal component (PC) scores from (A) the training data for hard bone, soft bone, muscle, fat, skin, and nerve (FR6 = 2.08–2.50 MHz). First three PC scores from (B) the testing data for hard bone, soft bone, muscle, fat, skin, and nerve (FR6 = 2.08–2.50 MHz). Receiver operating characteristic curve (C) to multiclass using the artificial neural network models combined with the ns-Nd:YAG laser. Note that the curve of hard bone, skin, muscle, and nerve tissues versus other tissues overlaps (FR6 = 2.08–2.50 MHz)